Supplementary Information
Parametric down-conversion photon-pair source on a nanophotonic chip

Xiang Guo, Chang-Ling Zou, Carsten Schuck, Hojoong Jung, Risheng Cheng, and Hong Tang
Department of Electrical Engineering, Yale University, New Haven, Connecticut 06511, USA

Contents

I. WRAP-AROUND WAVEGUIDE FOR HIGHER ORDER MODE EXCITATION

High frequency (visible wavelength) TM_2 mode and low frequency (IR wavelength) TM_0 mode are co-existing in the same microring resonator, as illustrated in Fig. S1a. We tune the visible pump laser into phase-matched resonance to excite corresponding TM_2 mode in microring resonator. Due to cavity enhanced $\chi^{(2)}$ effect, visible photons in TM_2 mode will be down converted to IR photon pairs in TM_0 mode. Critical coupling for visible TM_2 mode is desired to maximize pump power inside microring cavity and hence the photon pair generation efficiency (Supplementary section III). To maintain the high Q for IR modes, however, the visible light coupling waveguide cannot be too close to the microring. We therefore adopt a very narrow wrap-around waveguide for visible light coupling. Efficient TM_2 mode excitation is achieved when the effective refractive index of fundamental TM_0 mode in wrap-around waveguide matches that of TM_2 mode in the microring resonator.

Visible light TM_2 mode's effective refractive index is $n_{TM_2} = 1.988$ with $w = 1.10\,\mu$m, as shown in Fig. 1b in main context. Considering the radius difference, the phase match condition requires the targeted effective index of the wrap-around waveguide should be $n_{TM_0} = n_{TM_2} \cdot \frac{R_{microring}}{R_{b\mu s}} = 1.988 \cdot \frac{30}{31} = 1.9239$. The waveguide width is determined to be $w = 70\,$nm according to numerical simulation. In reality, however, this phase match condition is not strict because critical coupling only requires small coupling efficiency (on the order of 1%). We use a tapered wrap-around waveguide design, e.g. from 150 nm to 100 nm, for better fabrication robustness. We simulate coupling region taking into account bending effect due to the microring curvature (Fig. S1b). It is clear that the TM_2 mode can be effectively excited with tapered narrow waveguide. Coupling efficiency with different bus waveguide widths and different gap values is simulated with coupling length fixed to be $80\,\mu$m, as shown in Fig. S1c. We find that critical coupling gap can be quite large when choosing proper wrap-around waveguide width. For example, critical coupling could be achieved with a gap of $0.5\,\mu m$ with a wrap-around waveguide tapering from 150 nm to 100 nm. The device shown in the main context is slightly under-coupled with relative small resonance extinction. A near critically-coupled transmission spectrum is shown in Fig. S1e. The resonances fitted with red lines correspond to TM_2 mode. A critically coupled Q for TM_2 mode near 775 nm is measured to be 7×10^4.

The existence of wrap-around waveguide may induce extra scattering for IR photons and deteriorate Q for IR modes. We numerically calculated scattering Q induced by the wrap-around waveguide assuming a microring radius of $30\,\mu$m, as shown in Fig. S1d. The scattering Q is around 2.7×10^6 with a gap of $0.5\,\mu m$, much bigger than the critically coupled IR Q of 2×10^5. Hence we conclude that the existence of wrap-around waveguide will not degrade the Q of IR modes.

II. WAVEGUIDE COUPLED SUPERCONDUCTING SINGLE PHOTON DETECTOR

We use superconducting single-photon detectors (SSPD) to measure the statistical properties of the light field and extract correlations between photon detection events. The SSPDs are fabricated in traveling wave geometry on top of SiN waveguide-devices on a separate silicon chip inside a cryostat at 1.7 K. Each SSPD is realized as a U-shaped $40\,\mu$m long, 70 nm narrow and 8 nm thin NbTiN nanowire. This SSPD design realizes more than 95% photon absorption efficiency, milli-Hz dark count rate and high timing accuracy.

The on-chip detection efficiency for a representative device is shown in Fig. S2c as a function of SSPD bias current for photons of 1550 nm wavelength. For all SSPDs used here we observe around 14% on-chip detection efficiency when biased close to the critical current, I_c. We measured a system detection efficiency of 0.7% considering insertion loss from fiber to chip and calibration outputs. The grating couplers used for guiding light from the output of an optical fiber into the waveguides on chip show some wavelength dependency, as seen from Fig. S2d. The transmission spectrum is centered at 1550 nm and translates directly to system detection efficiency as the intrinsic quantum efficiency of an SSPDs only varies negligibly for small wavelength changes around 1550 nm.

We use the device shown in Fig S2a to measure self-correlations of degenerate down conversion and the idler of the nearest non-degenerate down conversion. Photons are coupled onto the chip via one of the central two input grating couplers, split randomly at a 50/50 directional coupler (center) and are detected at its outputs. To measure cross-correlations between signal and idler photons in the non-degenerate case we use the device shown in Fig S2b. Here photons are guided to the SSPDs via independent optical waveguides from the two outermost grating couplers.

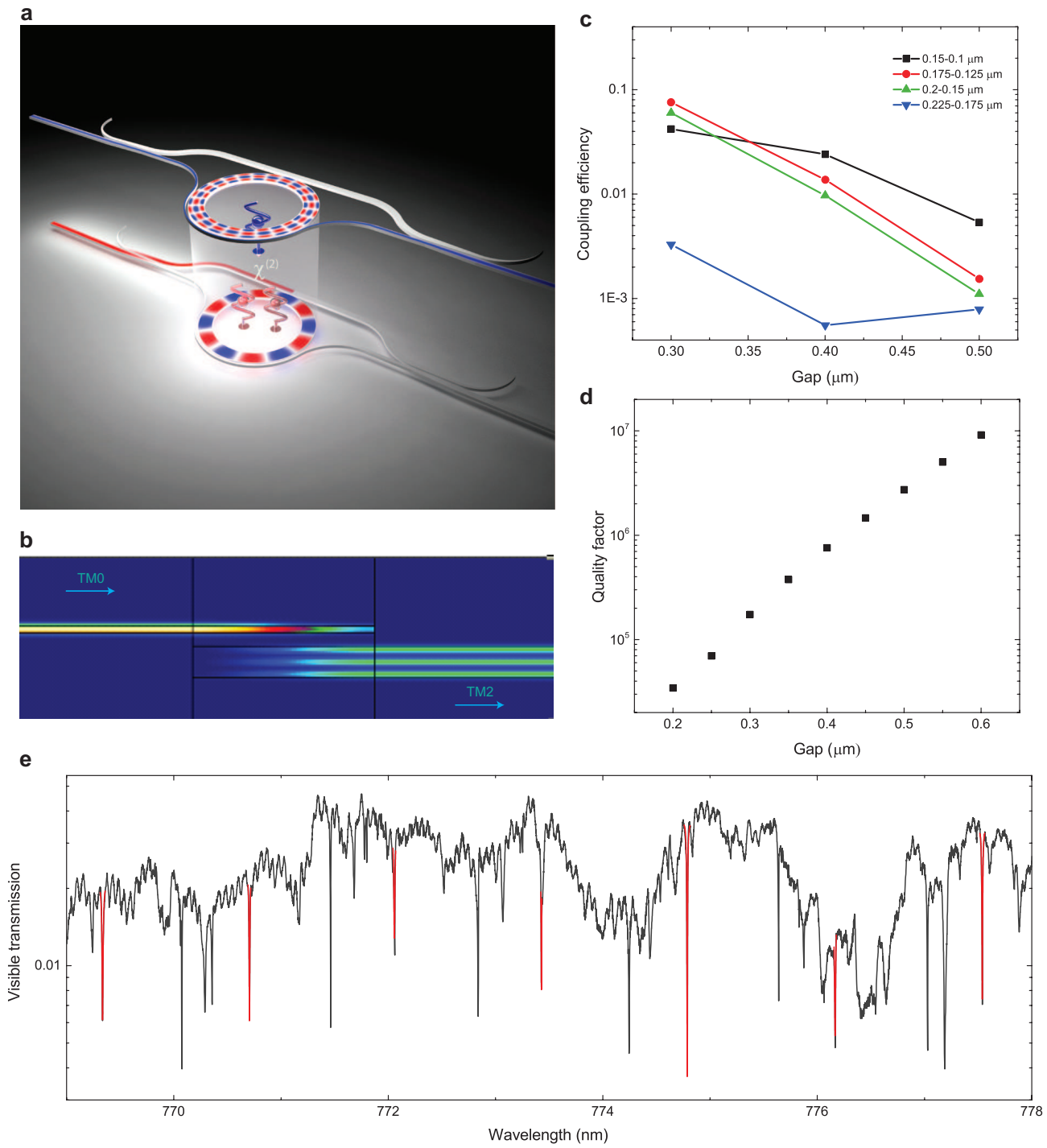

FIG. S1: **Triply-resonant parametric down conversion process in a microring resonator and wrap-around narrow waveguide for TM_2 mode excitation. a,** A schematic showing the parametric down conversion process in a triply resonant microring resonator. The high energy photon (blue) are coupled into TM_2 mode through wrap-around narrow waveguide and down converted to low frequency photon pairs (red) in TM_0 mode. The generated photon pairs are finally coupled out by the point-contact bus waveguide. The nodes number in the figure is arbitrary. For the real device, nodes number is around 484 for TM_2 mode near 775 nm. **b,** Intensity profile of visible light ($\lambda = 775$ nm) in the wrap-around waveguide coupling region. **c,** Simulated coupling efficiency for different bus waveguide width and gap values, with fixed coupling length to be 80 μm. The bending effect has been taken into consideration by defining effective curvature in the mode solver. **d,** Simulated scattering Q for IR modes induced by the scattering of wrap-around waveguide. **e,** A critically-coupled visible light transmission spectrum. The resonances fitted with red lines are TM_2 modes.

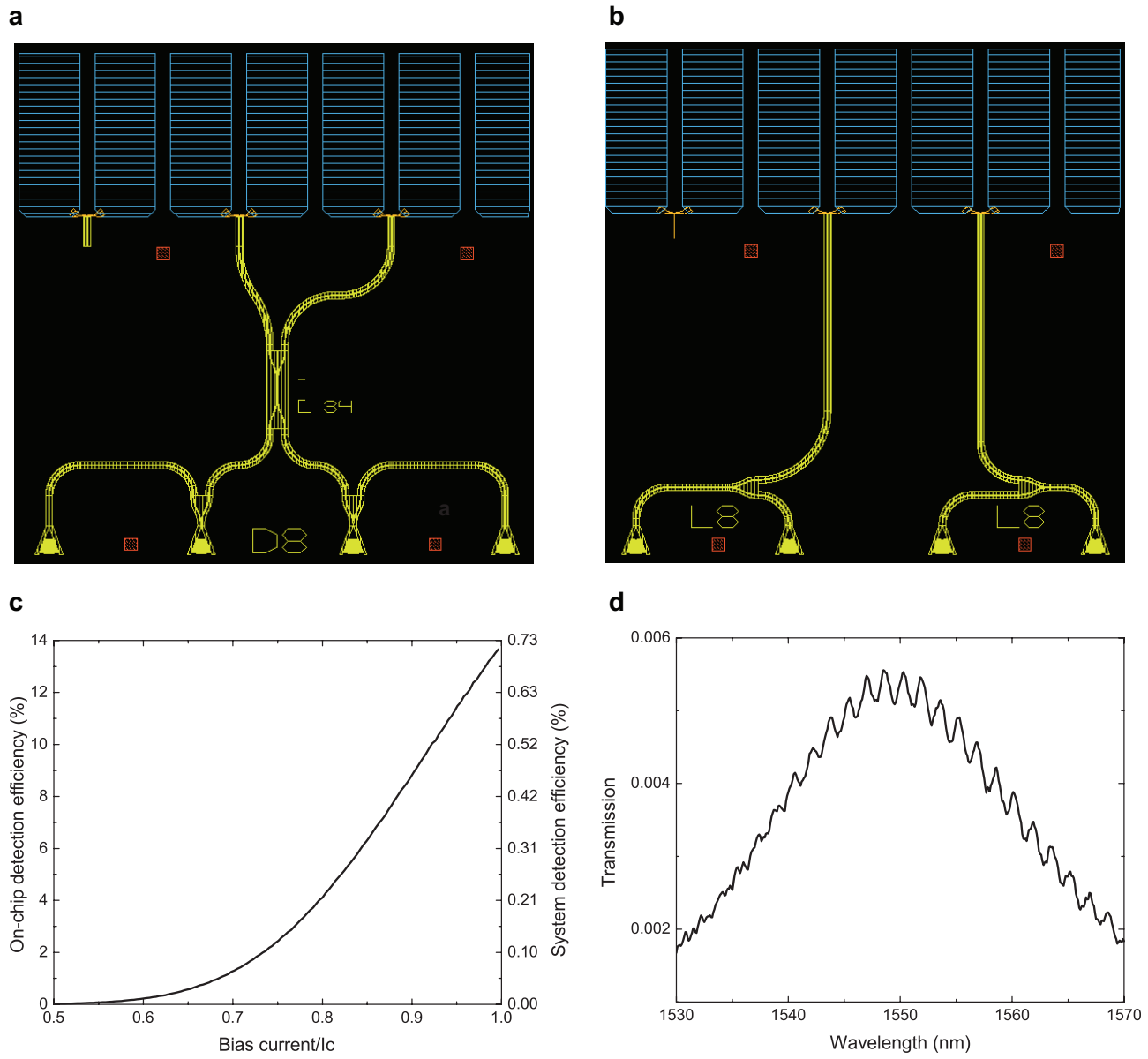

FIG. S2: **Waveguide coupled superconducting single photon detectors (SSPDs). a,** SSPDs with 50/50 directional coupler. **b,** SSPDs without directional coupler. **c,** On-chip and off-chip detection efficiency under different bias current. During measurement the bias current is set to be 95% of the critical current I_c. **d,** Transmission spectrum of the device.

III. $\chi^{(2)}$ IN THE MICRORING RESONATOR

A. Basics of $\chi^{(2)}$ process

In general, the second order nonlinear optics ($\chi^{(2)}$) process can be describe by the Hamiltonian

$$H = 2g(a^\dagger bc + ab^\dagger c^\dagger), \tag{S.1}$$

where a, b and c denote the Bosonic operator of three optical modes which satisfy the energy and momentum conservation relation. The factor of 2 is due to the non-degenerate process ($b \neq c$). Here g is the nonlinear coupling

strength proportional to material's second order nonlinear coefficient ($\chi^{(2)}$) as well as the mode overlap, with expression

$$g = \frac{\sqrt{\hbar}\sqrt{\omega_a\omega_b\omega_c}}{\sqrt{\varepsilon_0 2\pi R}} \frac{\int drdz\chi^{(2)}u_a(r,z)u_b^*(r,z)u_c^*(r,z)}{(\int drdzn_a^2(r,z)u_a^*(r,z)u_a(r,z))^{\frac{1}{2}}(\int drdzn_b^2(r,z)u_b^*(r,z)u_b(r,z))^{\frac{1}{2}}(\int drdzn_c^2(r,z)u_c^*(r,z)u_c(r,z))^{\frac{1}{2}}} \tag{S.2}$$

where ω_x is the angular frequency, n_x is refractive index and u_x is mode profile of mode x, x can be a, b, c. R is the radius of microring resonator. For different experiment with different pump and signal modes, we have a general table for $\chi^{(2)}$ processes [Table. I]. Therefore, we know that these processes share the same coupling strength g and are related in experiments. In our experiment, we mainly focus on the degenerate and non-degenerate SPDC processes, while using the second harmonic and difference frequency generation experiments to characterize the $\chi^{(2)}$ process and estimate the coupling strength g.

Name	Hamiltonian	Description
Sum-frequency	$H = 2g(a^\dagger bc + ab^\dagger c^\dagger) \approx 2g\langle b\rangle\langle c\rangle a^\dagger + h.c.$	pump at b and c, generate a
Second harmonic generation	$H = g[a^\dagger b^2 + a(b^\dagger)^2] \approx g\langle b\rangle^2 a^\dagger + h.c.$	$b = c$ degenerate, pump at b
Difference frequency generation	$H = 2g[a^\dagger bc + ab^\dagger c^\dagger] \approx 2g\langle a^\dagger b\rangle c + h.c.$	pump at a and b, generate c
Frequency Conversion	$H = 2g[a^\dagger bc + ab^\dagger c^\dagger] \approx 2g\langle b\rangle a^\dagger c + h.c.$	pump at b, signal is a or c
Non-degenerate SPDC	$H = 2g[a^\dagger bc + ab^\dagger c^\dagger] \approx 2g\langle a\rangle b^\dagger c^\dagger + h.c.$	pump at a
Degenerate SPDC	$H = g[a^\dagger b^2 + a(b^\dagger)^2] \approx g\langle a\rangle (b^\dagger)^2 + h.c.$	pump at a

TABLE I: Different $\chi^{(2)}$ nonlinear processes.

B. Second harmonic generation in microring resonator

For second harmonic generation process inside a microring resonator, the Hamiltonian [Table. I] can be written as

$$H = \omega_a a^\dagger a + \omega_b b^\dagger b + g[(a^\dagger)^2 b + a^2 b^\dagger] + i\epsilon_p(-ae^{i\omega_p t} + a^\dagger e^{-i\omega_p t}). \tag{S.3}$$

Here, $\omega_{a,b}$ are frequency of the IR and visible modes, $\epsilon_p = \sqrt{2\kappa_{a,1}\frac{P_p}{\hbar\omega_p}}$ corresponds to external pump laser with frequency ω_p and power P_p. $\kappa_{a,1}$ is the external coupling coefficient for the IR mode. The total amplitude decay rate of microring mode consists of intrinsic loss and external coupling as $\kappa_{a,tot} = \kappa_{a,0} + \kappa_{a,1}$, corresponding to a Q-factor as $Q = \frac{\omega_a}{2\kappa_{a,tot}}$. Similar parameters are used for visible mode by replacing the subscript a to b.

In the rotating frame of $A = \omega_p a^\dagger a + 2\omega_p b^\dagger b$, the Hamiltonian becomes

$$H = \delta_a a^\dagger a + \delta_b b^\dagger b + g((a^\dagger)^2 b + a^2 b^\dagger) + i\epsilon_p(-a + a^\dagger), \tag{S.4}$$

where $\delta_a = \omega_a - \omega_p$, $\delta_b = \omega_b - 2\omega_p$. Then, the dynamics of a can be solved by the Heisenberg equation

$$\frac{d}{dt}a = -i[a, H] - \kappa_{a,tot}a = (-i\delta_a - \kappa_{a,tot})a + \epsilon_p - ig2a^\dagger b \tag{S.5}$$

Under the non-depletion approximation, we omit last term. At steady state $da/dt = 0$, we have

$$a = \alpha = \left|\frac{-\epsilon_p}{-i\delta_a - \kappa_{a,tot}}\right| e^{i\theta} = \sqrt{\frac{2\kappa_{a,1}}{\delta_a^2 + \kappa_{a,tot}^2}}\sqrt{\frac{P_p}{\hbar\omega_p}}e^{i\theta}. \tag{S.6}$$

Here, θ is a phase factor depending on the driving laser. Treat a as complex constant α, and ignore the phase of α (as which can be combined into the phase of b), the Hamiltonian becomes

$$H = \delta_b b^\dagger b + g|\alpha|^2(b + b^\dagger) \tag{S.7}$$

Then, we can solve b as

$$\frac{d}{dt}b = (-i\delta_b - \kappa_{b,tot})b - ig|\alpha|^2. \tag{S.8}$$

At steady state, we have the generated second harmonic photon

$$b = \frac{ig\left|\alpha\right|^2}{-i\delta_b - \kappa_{b,tot}}. \tag{S.9}$$

Due to the input-output relation, the output is

$$b_{out} = -\sqrt{2\kappa_{b1}}b = \frac{-i\sqrt{2\kappa_{b1}}g\left|\alpha\right|^2}{-i\delta_b - \kappa_{b,tot}}. \tag{S.10}$$

The corresponding power of second harmonic output is

$$P_{SHG} = \left|b_{out}\right|^2\hbar\omega_b = g^2\frac{2\kappa_{b1}}{\delta_b^2+\kappa_{b,tot}^2}\left(\frac{2\kappa_{a,1}}{\delta_a^2+\kappa_{a,tot}^2}\right)^2\left(\frac{P_p}{\hbar\omega_p}\right)^2\hbar\omega_b. \tag{S.11}$$

The total second harmonic generation efficiency can be calculated as

$$\eta_{SHG} = \frac{P_{SHG}}{P_p^2} = g^2\frac{2\kappa_{b1}}{\delta_b^2+\kappa_{b,tot}^2}\left(\frac{2\kappa_{a,1}}{\delta_a^2+\kappa_{a,tot}^2}\right)^2\left(\frac{1}{\hbar\omega_p}\right)^2\hbar\omega_b \tag{S.12}$$

The momentum conservation (azimuthal quantum number conservation) is contained in the non-zero coupling strength g. The energy conservation condition is indicated by the efficiency that maximum efficiency can be achieved when $\delta_b = \delta_a = 0$, which requires $\omega_b = 2\omega_a$.

C. Degenerate SPDC

Now we consider the SPDC inside the microring resonator and start with the degenerate case. From Table. I, the Hamiltonian for degenerate SPDC is the same with the SHG, while with different pump laser frequency

$$H = \omega_a a^\dagger a + \omega_b b^\dagger b + g[(a^\dagger)^2 b + a^2 b^\dagger] + i\epsilon_s(-be^{i\omega_s t} + b^\dagger e^{-i\omega_s t}). \tag{S.13}$$

Here, $\omega_{a,b}$ are frequency of the IR and visible modes, $\epsilon_s = \sqrt{2\kappa_{b1}\frac{P_s}{\hbar\omega_s}}$ corresponds to external pump laser with frequency ω_s and power P_s. Similar to the SHG case, we solve the pump field under non-depletion and steady state approximations as

$$b = \beta = \sqrt{\frac{2\kappa_{b1}}{\kappa_{b,tot}^2+\delta_b^2}}\sqrt{\frac{P_s}{\hbar\omega_s}}e^{i\theta}, \tag{S.14}$$

where $\delta_b = \omega_b - \omega_s$ is the pump detuning of the mode b and θ is the phase depending on the driving. Treat b as complex constant β, and ignore the phase of β (as which can be combined into the phase of a), the Hamiltonian becomes

$$H = \delta_a a^\dagger a + g\left|\beta\right|[(a^\dagger)^2 + a^2], \tag{S.15}$$

with $\delta_a = \omega_a - \frac{\omega_s}{2}$.

For the SPDC, the vacuum noise plays great role to induce the spontaneous photon pair generation. Therefore, we solve the dynamics of IR photons with vacuum noise. The Langevin equation reads

$$\frac{d}{dt}a = (-i\delta_a - \kappa_{a,tot})a - i2g\left|\beta\right|a^\dagger - i\sqrt{2\kappa_{a,tot}}a_{in}, \tag{S.16}$$

where a_{in} is vacuum noise including all channels. Introducing the Fourier transformed operators as

$$a(\omega) = \frac{1}{2\pi}\int dt e^{-i\omega t}a(t), \tag{S.17}$$

$$a^\dagger(-\omega) = \frac{1}{2\pi}\int dt e^{-i\omega t}a^\dagger(t), \tag{S.18}$$

we have

$$0 = [-i(\delta_a + \omega) - \kappa_{a,tot}]a(\omega) - i2g\left|\beta\right| a^\dagger(-\omega) - i\sqrt{2\kappa_{a,tot}}a_{in}(\omega). \tag{S.19}$$

Then, we can solve

$$a(\omega) \;=\; \frac{i\sqrt{2\kappa_{a,tot}}\cdot[i(\delta_a-\omega)-\kappa_{a,tot}]a_{in}(\omega)+2g\left|\beta\right|\sqrt{2\kappa_{a,tot}}a_{in}^\dagger(-\omega)}{[i(\delta_a-\omega)-\kappa_{a,tot}]\cdot[-i(\delta_a+\omega)-\kappa_{a,tot}]-4g^2\left|\beta\right|^2}. \tag{S.20}$$

$$a^\dagger(-\omega) \;=\; \frac{-i\sqrt{2\kappa_{a,tot}}\cdot[-i(\delta_a+\omega)-\kappa_{a,tot}]a_{in}^\dagger(-\omega)+2g\left|\beta\right|\sqrt{2\kappa_{a,tot}}a_{in}(\omega)}{[-i(\delta_a+\omega)-\kappa_{a,tot}]\cdot[i(\delta_a-\omega)-\kappa_{a,tot}]-4g^2\left|\beta\right|^2}. \tag{S.21}$$

The output photon number spectrum density around mode a is:

$$S_{a,out}(\omega,\omega') \;=\; 2\kappa_{a,1}\left\langle a^\dagger(\omega)a(\omega')\right\rangle. \tag{S.22}$$

Due to the noise spectrum

$$\left\langle a_{in}^\dagger(t)a_{in}(t')\right\rangle = 0, \tag{S.23}$$

$$\left\langle a_{in}(t)a_{in}^\dagger(t')\right\rangle = \delta(t-t'), \tag{S.24}$$

and

$$\left\langle a_{in}^\dagger(\omega)a_{in}(\omega')\right\rangle = 0, \tag{S.25}$$

$$\left\langle a_{in}(\omega)a_{in}^\dagger(-\omega')\right\rangle = \frac{1}{2\pi}\delta(\omega+\omega'), \tag{S.26}$$

we finally obtain

$$\begin{aligned} S_{a,out}(\omega,\omega') \;=\; & \frac{1}{2\pi}\cdot 2\kappa_{a,1}\cdot\delta(\omega'-\omega)\cdot\frac{2g\left|\beta\right|\sqrt{2\kappa_{a,tot}}}{\left\{[-i(\delta_a-\omega)-\kappa_{a,tot}][i(\delta_a+\omega)-\kappa_{a,tot}]-4g^2\left|\beta\right|^2\right\}} \\ & \cdot\frac{2g\left|\beta\right|\sqrt{2\kappa_{a,tot}}}{\left\{[i(\delta_a-\omega')-\kappa_{a,tot}][-i(\delta_a+\omega')-\kappa_{a,tot}]-4g^2\left|\beta\right|^2\right\}} \end{aligned} \tag{S.27}$$

When input pump power below the threshold of optical parametric oscillator, we have $\left|\frac{4g^2|\beta|^2}{\delta_a^2+\kappa_{a,tot}^2}\right| \ll 1$, then

$$S_{a,out}(\omega,\omega') \;\approx\; \frac{\frac{1}{2\pi}\cdot 2\kappa_{a,1}(2g\left|\beta\right|\sqrt{2\kappa_{a,tot}})^2\cdot\delta(\omega'-\omega).}{\{[-i(\delta_a-\omega)-\kappa_{a,tot}][i(\delta_a+\omega)-\kappa_{a,tot}]\}\{[i(\delta_a-\omega')-\kappa_{a,tot}][-i(\delta_a+\omega')-\kappa_{a,tot}]\}} \tag{S.28}$$

The output photon rate is

$$\begin{aligned} N_{a,out} &= 2\kappa_{a,1}\left\langle a^\dagger(t)a(t)\right\rangle \\ &= \int d\omega d\omega' S_{a,out}(\omega,\omega')e^{i(\omega'-\omega)t} \\ &= \frac{1}{2\pi}\int d\omega\frac{2\kappa_{a,1}(2g\left|\beta\right|\sqrt{2\kappa_{a,tot}})^2}{\left|[-i(\delta_a-\omega)-\kappa_{a,tot}][i(\delta_a+\omega)-\kappa_{a,tot}]\right|^2} \\ &= \frac{4g^2\kappa_{a,1}}{\kappa_{a,tot}^2+\delta_a^2}\frac{2\kappa_{b1}}{\kappa_{b,tot}^2+\delta_b^2}\frac{P_s}{\hbar\omega_s}. \end{aligned} \tag{S.29}$$

The total photon generation rate is

$$\begin{aligned} N_a &= 2\kappa_{a,tot}\left\langle a^\dagger(t)a(t)\right\rangle \\ &= \frac{4g^2\kappa_{a,tot}}{\kappa_{a,tot}^2+\delta_a^2}\frac{2\kappa_{b1}}{\kappa_{b,tot}^2+\delta_b^2}\frac{P_s}{\hbar\omega_s}. \end{aligned} \tag{S.30}$$

In terms of photon pair, the total photon pair generation rate is

$$\begin{aligned} R &= N_a/2 \\ &= \frac{2g^2\kappa_{a,tot}}{\kappa_{a,tot}^2+\delta_a^2}\frac{2\kappa_{b1}}{\kappa_{b,tot}^2+\delta_b^2}\frac{P_s}{\hbar\omega_s}. \end{aligned} \tag{S.31}$$

D. Non-degenerate SPDC

For non-degenerate case, we introduce IR signal and idle modes as a and c, then the Hamiltonian is

$$\begin{aligned} H &= \omega_a a^\dagger a + \omega_b b^\dagger b + \omega_c c^\dagger c + 2g(a^\dagger b c^\dagger + a b^\dagger c) \\ &\quad + i\epsilon_s(-b e^{i\omega_s t} + b^\dagger e^{-i\omega_s t}). \end{aligned} \tag{S.32}$$

With other symbols similar to previous section, and under the non-depletion and steady state approximations, the Hamiltonian is simplified as

$$H = \delta_a a^\dagger a + \delta_c c^\dagger c + 2g\,|\beta|\,(a^\dagger c^\dagger + ac), \tag{S.33}$$

with $\delta_b = \omega_b - \omega_s$, $\delta_a + \delta_c = \omega_a + \omega_c - \omega_s$. The Langevin equations of a, c are

$$\frac{d}{dt}a = (-i\delta_a - \kappa_{a,tot})a - i2g\,|\beta|\,c^\dagger - i\sqrt{2\kappa_{a,tot}}a_{in}, \tag{S.34}$$

$$\frac{d}{dt}c = (-i\delta_c - \kappa_{c,tot})c - i2g\,|\beta|\,a^\dagger - i\sqrt{2\kappa_{c,tot}}c_{in}. \tag{S.35}$$

By Fourier transformation, we solve the equations

$$0 = [-i(\delta_a + \omega) - \kappa_{a,tot}]a(\omega) - i2g\,|\beta|\,c^\dagger(-\omega) - i\sqrt{2\kappa_{a,tot}}a_{in}(\omega), \tag{S.36}$$

$$0 = [-i(\delta_c + \omega) - \kappa_{c,tot}]c(\omega) - i2g\,|\beta|\,a^\dagger(-\omega) - i\sqrt{2\kappa_{c,tot}}c_{in}(\omega). \tag{S.37}$$

and obtain

$$a(\omega) = \frac{i\sqrt{2\kappa_{a,tot}}[i(\delta_c - \omega) - \kappa_{c,tot}]a_{in}(\omega) + 2g\,|\beta|\,\sqrt{2\kappa_{c,tot}}c_{in}^\dagger(-\omega)}{[-i(\delta_a + \omega) - \kappa_{a,tot}][i(\delta_c - \omega) - \kappa_{c,tot}] - 4g^2\,|\beta|^2}, \tag{S.38}$$

$$c^\dagger(-\omega) = \frac{-i\sqrt{2\kappa_{c,tot}}[-i(\delta_a + \omega) - \kappa_{a,tot}]c_{in}^\dagger(-\omega) + 2g\,|\beta|\,\sqrt{2\kappa_{a,tot}}a_{in}(\omega)}{[-i(\delta_a + \omega) - \kappa_{a,tot}][i(\delta_c - \omega) - \kappa_{c,tot}] - 4g^2\,|\beta|^2}. \tag{S.39}$$

Then, the output spectrum densities are

$$\begin{aligned} S_{a,out}(\omega,\omega') &= \frac{1}{2\pi}\cdot 2\kappa_{a,1}\cdot\delta(\omega'-\omega)\cdot\frac{2g\,|\beta|\,\sqrt{2\kappa_{c,tot}}}{\left\{[i(\delta_a+\omega)-\kappa_{a,tot}][-i(\delta_c-\omega)-\kappa_{c,tot}]-4g^2\,|\beta|^2\right\}} \\ &\quad\cdot\frac{2g\,|\beta|\,\sqrt{2\kappa_{c,tot}}}{\left\{[-i(\delta_a+\omega')-\kappa_{a,tot}][i(\delta_c-\omega')-\kappa_{c,tot}]-4g^2\,|\beta|^2\right\}} \end{aligned} \tag{S.40}$$

$$\begin{aligned} S_{c,out}(\omega,\omega') &= \frac{1}{2\pi}\cdot 2\kappa_{c,1}\cdot\delta(\omega'-\omega)\cdot\frac{2g\,|\beta|\,\sqrt{2\kappa_{a,tot}}}{\left\{[i(\delta_a+\omega)-\kappa_{a,tot}][-i(\delta_c-\omega)-\kappa_{c,tot}]-4g^2\,|\beta|^2\right\}} \\ &\quad\cdot\frac{2g\,|\beta|\,\sqrt{2\kappa_{a,tot}}}{\left\{[-i(\delta_a+\omega')-\kappa_{a,tot}][i(\delta_c-\omega')-\kappa_{c,tot}]-4g^2\,|\beta|^2\right\}} \end{aligned} \tag{S.41}$$

Below the threshold of optical parametric oscillator, we have $\left|\frac{4g^2|\beta|^2}{(-i\delta_a-\kappa_{a,tot})(i\delta_c-\kappa_{c,tot})}\right| \ll 1$, then we have the total photon pair generation rate to be

$$R = \frac{8g^2(\kappa_{a,tot}+\kappa_{c,tot})}{(\kappa_{a,tot}+\kappa_{c,tot})^2+(\omega_a+\omega_c-\omega_s)^2}\frac{2\kappa_{b1}}{\kappa_{b,tot}^2+(\omega_b-\omega_s)^2}\frac{P_s}{\hbar\omega_s}. \tag{S.42}$$

The output photon rate for mode a and c are

$$N_{a,out} = \frac{\kappa_{a,1}}{\kappa_{a,tot}}R, \tag{S.43}$$

$$N_{c,out} = \frac{\kappa_{c,1}}{\kappa_{c,tot}}R, \tag{S.44}$$

Comparing Eq. (S.42) with Eq. (S.31), we conclude that non-degenerate SPDC rate is two times more efficient than degenerate SPDC, assuming the phase match condition are both fulfilled and quality factors of IR modes are the same.

E. Experiment estimation of SPDC efficiency

Assuming the phase match condition is perfectly fulfilled ($\delta_a = \delta_b = 0$), together with Eq. (S.12), we can estimate the degenerate photon pair generation rate from SHG efficiency as

$$\begin{aligned} R &= \frac{2g^2\kappa_{a,tot}}{\kappa_{a,tot}^2}\frac{2\kappa_{b1}}{\kappa_{b,tot}^2}\frac{P_s}{\hbar\omega_s} \\ &= \frac{\kappa_{a,tot}^3}{8\kappa_{a,1}^2}\eta_{SHG}P_s. \end{aligned} \tag{S.45}$$

Therefore, the SHG efficiency η_{SHG} can be used as a figure of merit to optimize the device performance. Strong SHG will occur when IR pump is tuned into phase matched resonance. A typical IR transmission around the phase-matched resonance and the corresponding SHG are shown in Fig. S3a and b. With 0.146 mW IR pump power on-chip, the maximum SHG is 24.8 nW. This corresponds to a SHG efficiency to be: $\eta_{SHG} = \frac{P_{SHG}}{P_p^2} = 1.16\,(\mathrm{W}^{-1})$.

By tuning the temperature, IR and visible resonance teeth will be shifted respectively. Experimentally a red shifting with increasing temperature is observed for both IR and visible resonances, with different coefficient. For IR mode, $\frac{d\lambda_{IR}}{dT} = 0.0216\,(\mathrm{nm/°C})$, while for visible mode $\frac{d\lambda_{vis}}{dT} = 0.01136\,(\mathrm{nm/°C})$. The fact that $\frac{d\lambda_{IR}}{dT} - 2\frac{d\lambda_{vis}}{dT} = -0.0011\,(\mathrm{nm/°C}) \neq 0$ means that the two resonance teeth will have relative shift with the change of temperature. Under a certain temperature, when the corresponding resonances are aligned ($\lambda_N = 2\lambda_{2N}$), maximum SHG will occur. The temperature dependence of SHG efficiency η_{SHG} is shown in Fig. S3c. Theoretically, with IR mode to be critically coupled ($\kappa_{a,tot} = 2\kappa_{a,1}$) and a loaded $Q = 197\,\mathrm{K}$, and a maximum SHG efficiency to be $\eta_{SHG} = 1.16\,(\mathrm{W}^{-1})$, the degenerate down conversion photon pair generation rate per unit pump power is calculated to be: $\frac{R}{P_s} = \frac{1}{2}\kappa_{a,tot}\eta_{SHG} = \frac{\omega_a}{4Q}\eta_{SHG} = 1.8\,(\mathrm{MHz/mW})$.

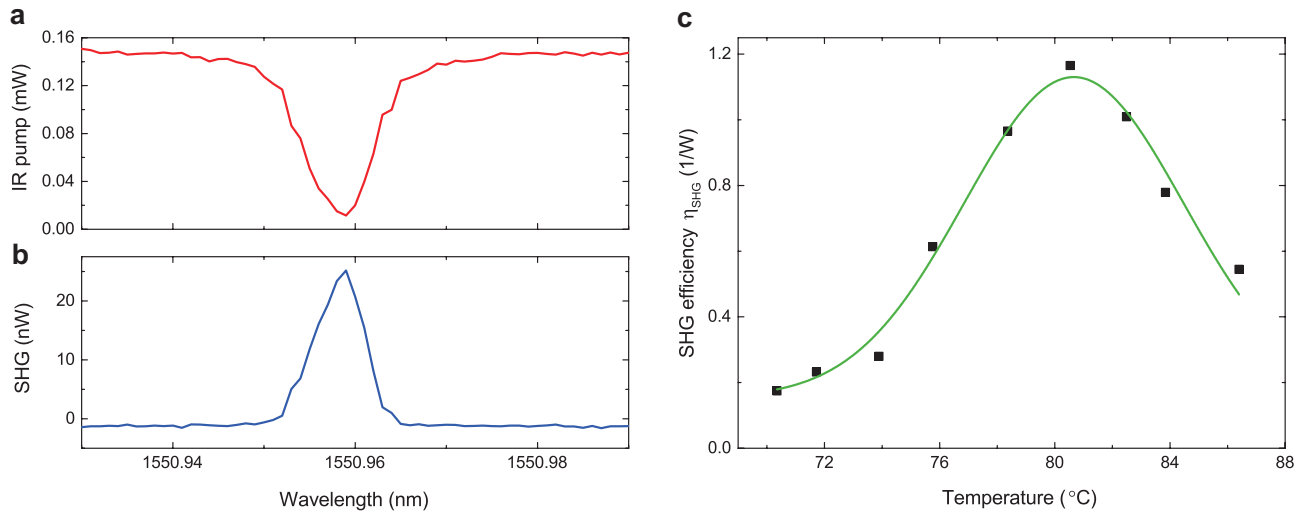

FIG. S3: **Second harmonic generation (SHG) in microring resonator.** **a,** IR transmission around phase-matched resonance. **b,** Measured SHG under different IR pump wavelength. **c,** SHG efficiency η_{SHG} under different temperature.

F. Raw data of coincidence measurement

The raw data of coincidence measurement for the nearest non-degenerate down conversion is shown in Fig. S4, with on-chip pump power of 1.9 mW. A coincidence time window of 128 ps is used to get the coincidence histogram. Due to the small jitter time of our SSPDs compared to the photon life time, the coincidence peak can be fully resolved. By summing up the coincidence under the peak, the total measured coincidence rate is around 80 Hz.

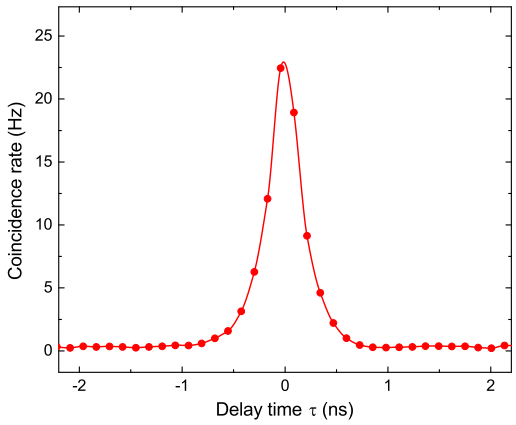

FIG. S4: **Raw data of coincidence measurement.** Here the binwidth is chosen to be 128 ps. The total measured coincidence rate is around 80 Hz.

IV. DISPERSION AND BANDWIDTH OF THE GENERATED DOWN-CONVERSION PHOTON COMBS

The waveguide width in our device is engineered so that phase match condition between TM_0 mode in IR and TM_2 mode in visible band will be fulfilled. The group velocity dispersion (GVD) for the IR mode is not optimized. Due to the non-zero GVD, the generated photon frequency comb will have a limited bandwidth. For our waveguide size, effective refractive index of TM_0 mode under different wavelength has been simulated. The fitting equation is $n_{eff} = 1.99139 - 0.2107 \cdot \Delta\lambda - 0.02837 \cdot \Delta\lambda^2$ (unit of $\Delta\lambda$ is μm), corresponding to a GVD of $D = -\frac{\lambda}{C}\frac{d^2n}{d\lambda^2} = 146\ \frac{\text{ps}}{\text{km}\cdot\text{nm}}$ around 1550 nm. Considering that the temperature is optimized so that the resonance teeth is aligned, the phase match condition for degenerate down conversion is perfectly fulfilled. Then we need to calculate how much detuning there is for the non-degenerate photon pairs whose wavelength is $\delta\lambda$ away from the degenerate down conversion photon wavelength. The detuning $\Delta\omega$ can be expressed with D as

$$\Delta\omega = \omega_a + \omega_c - \omega_b = \frac{\omega^2 (\delta\lambda)^2}{2\pi n_g} \cdot D \tag{S.46}$$

Let $\Delta\omega = \kappa_{a,tot} + \kappa_{c,tot}$ (Considering IR modes are critically coupled with loaded $Q = 197\,\text{K}$)

$$\Delta\omega = \frac{\omega^2 (\delta\lambda)^2}{2\pi n_g} \cdot D = \kappa_{a,tot} + \kappa_{c,tot} = \frac{\omega}{Q} \tag{S.47}$$

$$\delta\lambda = \sqrt{\frac{2\pi n_g}{\omega Q \cdot D}} = 20.2\,\text{nm} \tag{S.48}$$

From Eq. (S.42), when $\Delta\omega = \kappa_{a,tot} + \kappa_{c,tot}$, the SPDC generation rate will drop to half. Hence the full width at half maximum (FWHM) of the SPDC photon comb is $2 \cdot \delta\lambda = 40.4\,\text{nm}$.

V. THE SECOND ORDER CORRELATION FUNCTION $g^{(2)}(\tau)$

A. Photon correlation function

For non-degenerate down conversion cross correlation, $g^{(2)}(\tau)$ can be fitted by a double exponential function

$$g^{(2)}_{cross}(\tau) = 1 + \frac{1}{2R\tau_c} e^{-|\tau|/\tau_c}, \tag{S.49}$$

For degenerate down conversion self correlation, photons will be split randomly by the 50/50 directional coupler. There are 50% of chance that both photons go to the same detector and coincidence cannot be detected. So the peak value will drop by a factor of 2 and the $g^{(2)}(\tau)$ function can be fitted as

$$g^{(2)}_{self}(\tau) = 1 + \frac{1}{4R\tau_c} e^{-|\tau|/\tau_c}, \tag{S.50}$$

B. Detector jitter and bin-width's broadening effect on the $g^{(2)}(\tau)$ function

The detector's jitter means that the time recorded by the time-tagging electronics is not exactly the photon arrival time. This gives error on the time tagging data, thus affects the shape of the measured coincidence histogram. Another factor that will influence the width of coincidence histogram is the coincidence time window (bin-width) that is chosen to process the time tagging data. The bigger bin-width will give more uncertainty, resulting in a broader coincidence histogram. Uncertainty of arrival time due to photon lifetime together with the bin-width and detector jitter determine the width of the coincidence histogram distribution. To calibrate the detector jitter's effect, a down-conversion source based on short PPKTP waveguide is tested by our integrated photon correlation measurement system. Due to the broadband nature of the down-converted photons from short crystal waveguide, the intrinsic photon arrival time difference is within several ps, much shorter than the detector jitter. Thus the distribution of the coincidence histogram (Fig. S5) is almost fully due to the jitter and bin-width. Here the bin-width is chosen to be $\tau_b = 10\,\text{ps}$. The Gaussian fitting of the histogram gives the standard deviation to be $\tau_w = 26\,\text{ps}$. With the equation of $\tau_w = \sqrt{\left(\frac{\tau_b}{2}\right)^2 + 2\tau_j^2}$, the detector jitter is calculated to be $\tau_j = 18\,\text{ps}$. Due to jitter and bin-width, a sharp coincidence peak is transformed into a Gaussian distribution. For photons generated from the microring resonator whose photon life time is comparable to the jitter and bin-width, the measured $g^{(2)}$ function is actually the convolution between original double exponential function due to the source property and the Gaussian distribution

$$\begin{aligned} g^{(2)}_{self}(\tau) &= [1 + \frac{1}{4R\tau_c} e^{-|\tau|/\tau_c}] * [\frac{1}{\sqrt{2\pi}\tau_w} e^{-\tau^2/2\tau_w^2}] \\ &= 1 + \frac{1}{8R\tau_c} e^{\tau_w^2/2\tau_c^2} \left[f_+(\tau) + f_-(\tau)\right], \end{aligned} \tag{S.51}$$

$$\begin{aligned} g^{(2)}_{cross}(\tau) &= [1 + \frac{1}{2R\tau_c} e^{-|\tau|/\tau_c}] * [\frac{1}{\sqrt{2\pi}\tau_w} e^{-\tau^2/2\tau_w^2}] \\ &= 1 + \frac{1}{4R\tau_c} e^{\tau_w^2/2\tau_c^2} \left[f_+(\tau) + f_-(\tau)\right], \end{aligned} \tag{S.52}$$

where $f_\pm(\tau) = \left[1 \mp \text{erf}\left(\frac{\tau \pm \tau_w^2/\tau_c}{\sqrt{2}\tau_w}\right)\right] \cdot e^{\pm\tau/\tau_c}$.

C. Cross correlation for other two groups of photon pairs

Cross correlation of the other two neighboring photon-pair group has also been measured. The measurement result is shown in Fig. S6. A 50/50 fiber-coupler is used to randomly split the photon flux into two arms. Tunable filters are inserted in both arms. By tuning the passband of the each bandpass filter, the signal and idler could be selected and the coincidence is measured by two separate waveguide coupled SSPDs.

VI. ADIABATIC ON-CHIP WAVELENGTH DIVISION MULTIPLEXER (WDM)

The designed on-chip WDM is shown in the Fig. 5 in the main context, which consists of two tapered coupled waveguides. Shown in Fig. S7a is the cross section of such two waveguides, one with width $w_1 = w_0 - w$ and the other with $w_2 = w_0 + w$. Here $2w$ is the width difference of the two waveguides. We linearly tapered the two waveguides, with one waveguide tapered to be narrower, the other to be wider, with expressions: $w = (z - \frac{l_0}{2}) \cdot a$. Here z is the coordinate along the tapering direction, l_0 is the total length of the WDM device and a is the tapering speed. The gap between the two waveguides is fixed in the entire tapered structure, and the designed central waveguide width is $w_0 = 0.7\,\mu\text{m}$.

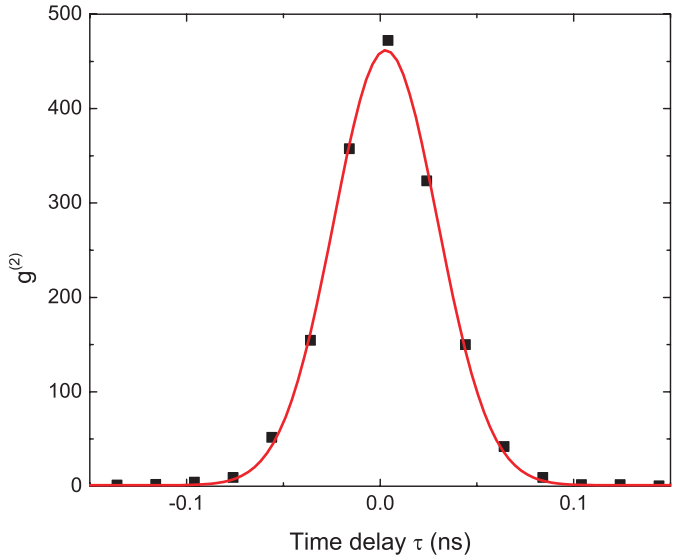

FIG. S5: **Second order correlation function of PPKTP waveguide down conversion source measured by on-chip SSPDs**

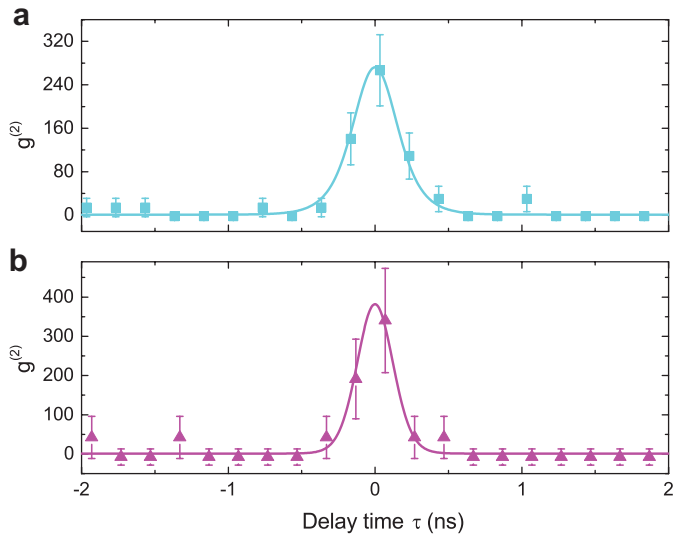

FIG. S6: **Second order cross correlation function for the second and third nearest non-degenerate down conversion photon pairs. a,** The second nearest non-degenerate photon pairs with $\lambda_{signal} = 1539.0\,\text{nm}$, $\lambda_{idler} = 1562.5\,\text{nm}$ **b,** The third nearest non-degenerate photon pairs with $\lambda_{signal} = 1532.9\,\text{nm}$, $\lambda_{idler} = 1568.6\,\text{nm}$. The binwidth is chosen to be 200 ps.

In the coupled waveguides, new eigenmodes formed as combination of eigenmodes in separated waveguides. The relationship between the new eigenmodes' effective refractive indices and the waveguide width difference $2w$ is shown in Fig. S7b and c. For wavelength of $\lambda = 1550\,\text{nm}$, The big avoided-crossing gap (Fig. S7b) indicates strong mode coupling for IR light. While for $\lambda = 775\,\text{nm}$, the avoided-crossing gap (Fig. S7c) is much smaller due to better light confinement in the waveguide and indicates weak coupling.

In this tapered coupled waveguide, the adiabatic mode coupling efficiency can be estimated by Lauder-Zener formula as

$$\zeta = 1 - e^{-\frac{\pi g^2 k l_0}{\Delta n}}, \tag{S.53}$$

where g is the coupling strength, $k = \frac{2\pi}{\lambda}$ is the wave vector, and Δn is the refractive index difference between the wide ($w_{wide} = 0.8\,\mu\text{m}$) and narrow ($w_{narrow} = 0.6\,\mu\text{m}$) waveguide. From the coupled mode theory, the coupling strength g between two waveguides can be deduced from the avoided-crossing gap as g equals to the half of the minimum

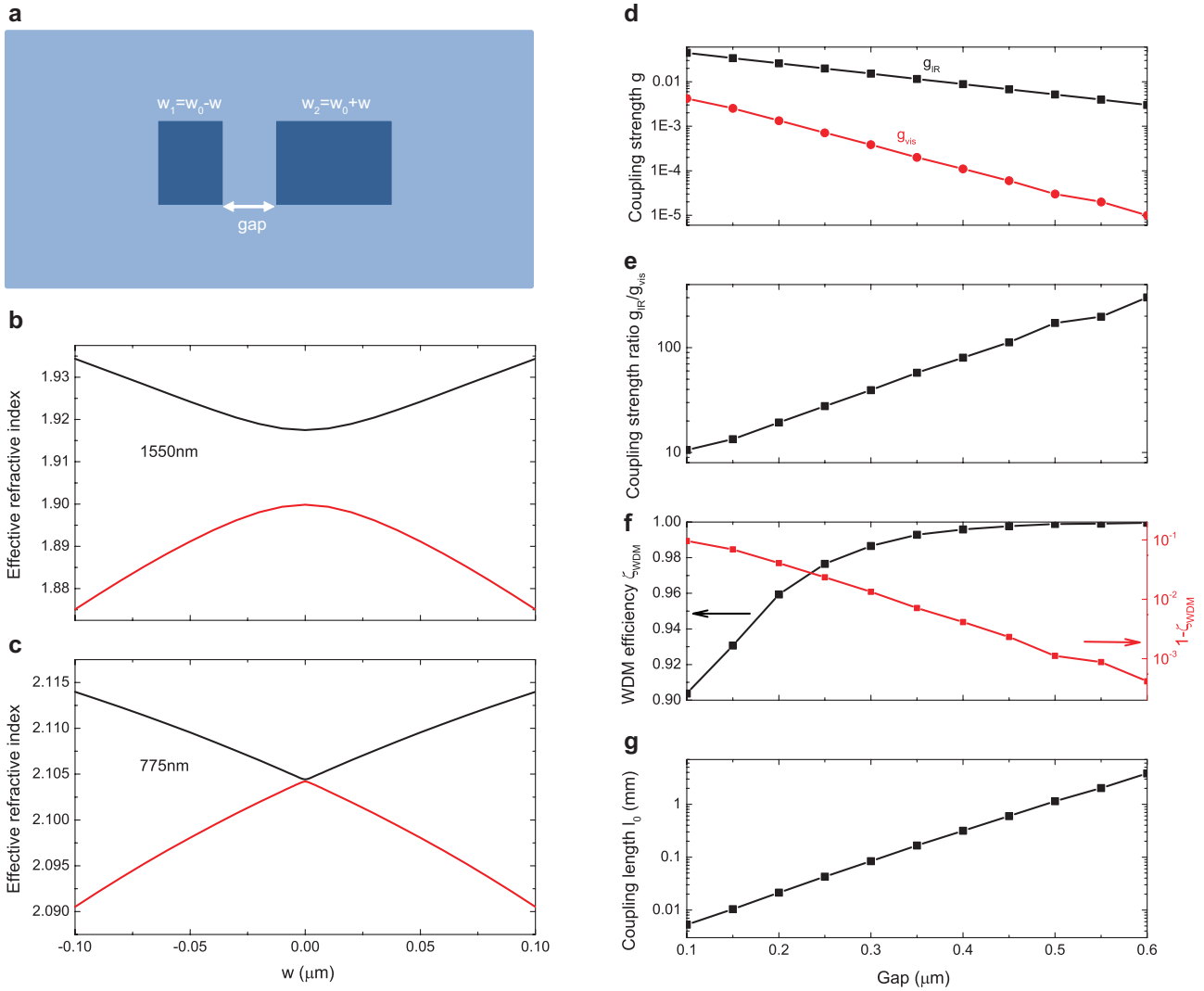

FIG. S7: **Adiabatic on-chip WDM. a,** Cross section of the WDM structure. The narrow waveguide width is $w_0 - w$ and wide waveguide $w_0 + w$. The gap is fixed throughout the structure. **b,** Effective refractive index for IR light ($\lambda = 1550\,\mathrm{nm}$) symmetric and anti-symmetric TM_0 modes when w varies from $-0.1\,\mu\mathrm{m}$ to $0.1\,\mu\mathrm{m}$. **c,** Effective refractive index of visible light ($\lambda = 775\,\mathrm{nm}$) symmetric and anti-symmetric TM_0 mode when w varies from $-0.1\,\mu\mathrm{m}$ to $0.1\,\mu\mathrm{m}$. **d,** Coupling strength g for both IR and visible light under different gap. Waveguide width w_0 is $0.7\,\mu\mathrm{m}$. **e,** Coupling strength ratio $\frac{g_{IR}}{g_{vis}}$ between IR and visible light. **f,** The optimized WDM efficiency under different gap values. WDM efficiency ζ_{WDM} stands for cross port coupling efficiency for IR, and drop port coupling efficiency for visible. **g,** The coupling length needed to achieve best WDM performance.

refractive index difference. The big difference in coupling strength g leads to different performances of the same structure under difference wavelengths. With IR light passing through the structure, adiabatic mode coupling will happen in the avoided-crossing region and light's energy is coupled to the other waveguide gradually. With visible light input, the photons goes through the avoided-crossing region non-adiabatically and most of photons will still remain in the same waveguide after the coupling region. Mathematically, for IR modes whose $\frac{\pi g^2 k l_0}{\Delta n} \gg 1$, ζ will approach unity with the increase of l_0. For visible mode whose $\frac{\pi g^2 k l_0}{\Delta n} \ll 1$, $\zeta \approx \frac{\pi g^2 k l_0}{\Delta n}$ will be a small value close to 0 and linearly dependent on l_0. These explained the two curves in Fig. 5c in the main context.

We design the structure as an efficient on-chip WDM between IR and visible light. Because we want to make IR's cross coupling to be as high as possible, while keeping visible light's cross coupling to be as low as possible, the figure of merit that needs to be optimize is the ratio between IR coupling strength g_{IR} and visible light coupling strength $g_{visible}$: $\frac{g_{IR}}{g_{visible}}$. As coupling between waveguides are weaker with bigger gap, both IR and visible light coupling strength (g_{IR} and g_{vis}) will decrease with the gap (Fig. S7d). However, the coupling strength ratio $\frac{g_{IR}}{g_{visible}}$

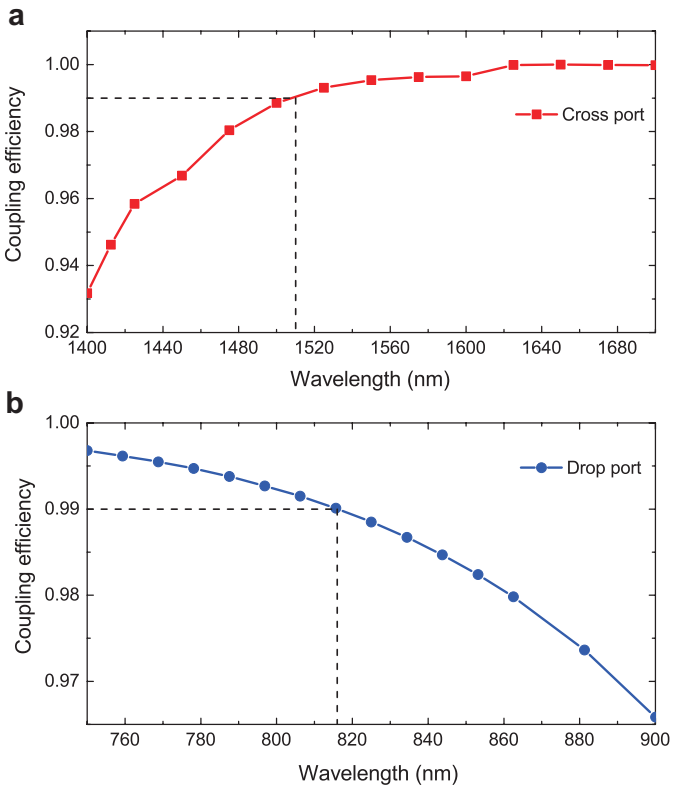

FIG. S8: **Wavelength dependent coupling efficiency for on-chip WDM. a,** Cross port coupling efficiency for IR light. For IR light whose wavelength $\lambda \geq 1510\,\text{nm}$, cross port coupling efficiency is higher than 99%. **b,** Drop port coupling efficiency for visible light. For visible light whose wavelength $\lambda \leq 816\,\text{nm}$, drop port coupling efficiency is higher than 99%.

will increase monotonically with the gap as shown in Fig. S7e. Let IR's crossing coupling to be equal with visible's drop coupling, with equation: $\zeta_{IR} = 1 - \zeta_{visible}$, we can calculate the optimized coupling length l_0 and corresponding WDM efficiency ζ_{WDM} $(= \zeta_{IR} = 1 - \zeta_{visible})$. The WDM efficiency ζ will increase with gap and approach unity (Fig. S7f). However, the corresponding coupling length l_0 will also increase with gap (Fig. S7g). Considering the footprint and the propagation loss in the waveguide, the WDM's length l_0 cannot be arbitrarily long. WDM efficiency ζ_{WDM} is greater than 99.9% with $0.55\,\mu$m gap and 2 mm coupling length. This performance corresponds to 30 dB isolation of visible light with 0.004 dB insertion loss for IR light for each WDM.

We also expects a broad-band operation from the robust performance of the on-chip WDM. The wavelength dependence of coupling efficiency is shown in Fig. S8 with the following design parameters: $w_{wide} = 0.8\,\mu$m, $w_{narrow} = 0.6\,\mu$m, $gap = 0.4\,\mu$m, $l_0 = 260\,\mu$m. For IR light with wavelength $\lambda \geq 1510\,\text{nm}$, cross port coupling efficiency is more than 99%. For visible light with wavelength $\lambda \leq 816\,\text{nm}$, drop port coupling efficiency is more than 99%.